

Laser-Induced Positional and Chemical Lattice Reordering Generating Ferromagnetism

Theo Pflug,* Javier Pablo-Navarro, Md. Shabad Anwar, Markus Olbrich, César Magén, Manuel Ricardo Ibarra, Kay Potzger, Jürgen Faßbender, Jürgen Lindner, Alexander Horn, and Rantej Bali

Atomic scale reordering of lattices can induce local modulations of functional material properties, such as reflectance and ferromagnetism. Pulsed femtosecond laser irradiation enables lattice reordering in the picosecond range. However, the dependence of the phase transitions on the initial lattice order as well as the temporal dynamics of these transitions remain to be understood. This study investigates the laser-induced atomic reordering and the concomitant onset of ferromagnetism in thin Fe-based alloy films with vastly differing initial atomic orders. The optical response to single femtosecond laser pulses on selected prototype systems, one that initially possesses positional disorder, $\text{Fe}_{60}\text{V}_{40}$, and a second system initially in a chemically ordered state, $\text{Fe}_{60}\text{Al}_{40}$, has been tracked with time. Despite the vastly different initial atomic orders the structure in both systems converges to a positionally ordered but chemically disordered state, accompanied by the onset of ferromagnetism. Time-resolved measurements of the transient reflectance combined with simulations of the electron and phonon temperatures reveal that the reordering processes occur via the formation of a transient molten state with an approximate lifetime of 200 ps. These findings provide insights into the fundamental processes involved in laser-induced atomic reordering, paving the way for controlling material properties in the picosecond range.

arrangement of the lattice points and the compositional order of the atomic species within the lattice.^[1–4] Order in alloy lattices can be classified by the degree to which the atoms form a periodic lattice, in terms of preserving specific bond distances as well as the compositional sequence in which the atoms are arranged. Deviations in the bond distances or a break in the compositional sequence lead to aperiodicity, which can cause drastic changes in intrinsic behavior. There exists a continuous range of ordering, from perfect ordering in single crystals to a complete randomization of the lattice, and in alloy systems, disordering can take complex intermediate forms. This study attempts to delineate the following two types of order in lattices (see **Figure 1**). Positional order refers to a well-defined, constant arrangement of lattice points over long distances with several lattice spacings.^[5,6] In contrast, positional disorder corresponds to lattice points randomly distributed in space. Analogous to positional (dis)order, chemical (dis)order refers to the periodicity of the atomic species occupying the lattice sites. In chemical order, atoms of

a given species are assigned to specific sites of the ordered lattice, whereby chemical disorder denotes the occupation of the lattice points by a random sequence of atomic species.^[6–8] This description results in a hierarchy through which chemical

1. Introduction

Functional properties of materials, including their optical and magnetic characteristics, are profoundly affected by the spatial


T. Pflug, M. Olbrich, A. Horn
Laserinstitut Hochschule Mittweida
Hochschule Mittweida
09648 Mittweida, Germany
E-mail: pflug@hs-mittweida.de

J. Pablo-Navarro, C. Magén, M. R. Ibarra
Instituto de Nanociencia y Materiales de Aragón (INMA)
CSIC-Universidad de Zaragoza
50018 Zaragoza, Spain

J. Pablo-Navarro, C. Magén, M. R. Ibarra
Laboratory of Advanced Microscopies (LMA)
University of Zaragoza
50018 Zaragoza, Spain

M. S. Anwar, K. Potzger, J. Faßbender, J. Lindner, R. Bali
Institute of Ion Beam Physics and Materials Research
Helmholtz-Zentrum Dresden-Rossendorf
01328 Dresden, Germany

M. S. Anwar, J. Faßbender
Institut für Festkörper- und Materialphysik
Technische Universität Dresden
01069 Dresden, Germany

 The ORCID identification number(s) for the author(s) of this article can be found under <https://doi.org/10.1002/adfm.202311951>

© 2023 The Authors. Advanced Functional Materials published by Wiley-VCH GmbH. This is an open access article under the terms of the Creative Commons Attribution-NonCommercial License, which permits use, distribution and reproduction in any medium, provided the original work is properly cited and is not used for commercial purposes.

DOI: 10.1002/adfm.202311951

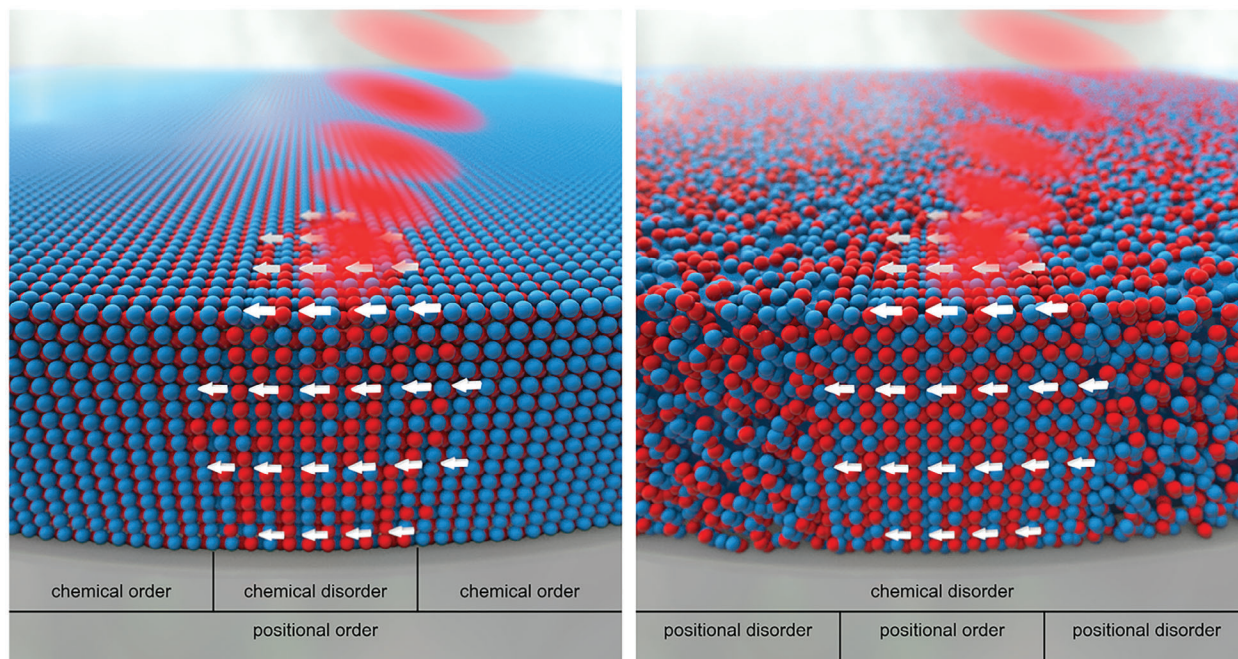


Figure 1. Schematic atomic structures of the investigated prototype alloys $\text{Fe}_{60}\text{Al}_{40}$ (left) and $\text{Fe}_{60}\text{V}_{40}$ (right). $\text{Fe}_{60}\text{Al}_{40}$ features a positional and chemical order before irradiation (left image), whereas $\text{Fe}_{60}\text{V}_{40}$ is positionally and chemically disordered (right image). After irradiation, both materials become positionally ordered with a chemical disorder of the lattice site occupancies (left and right irradiated area).

order can only exist if there is positional order. Subtle changes in both positional and chemical order have been demonstrated to yield significant modifications in the material's optical properties, for example, reflectance, as well as in the magnetic behavior, such as the exchange coupling, and can result in the onset of ferromagnetism.^[8–10]

These alterations to the functional material properties described above can be induced by single-pulsed femtosecond (fs) laser irradiation^[9] and can be tracked in the ultrafast time regime by applying pump-probe metrology.^[11–15] This approach provides insights into the pathways leading to lattice reordering. However, whereas single fs pulses have been applied to selected systems, the broader scope of the transformations in lattice order remains an open question, for example, the effect of single fs laser pulsing on different types of positional and chemical order and crucially, the time scales at which transformations can be realized.

In this study, laser-induced positional and chemical reordering is investigated in two prototype Fe-based alloys, possessing vastly different initial lattice states. The first alloy under examination, $\text{Fe}_{60}\text{Al}_{40}$, features a B2 crystal structure with well-defined positional and chemical order prior to irradiation (Figure 1, left). Its chemical order consists of pure Fe planes separated by Al-rich planes, resulting in a Fe–Fe nearest-neighbor coordination of 2.7, corresponding to a paramagnetic state.^[7,8,16,17] In contrast, the second alloy, $\text{Fe}_{60}\text{V}_{40}$, exhibits positional and chemical disorder in its initial state (Figure 1, right).^[10,18–21] By modifying the chemical order in both alloys through energy deposition via penetrating ions^[8,16,22–24] or laser irradiation,^[7,9,25] a formation into a positionally ordered but chemically disordered state, referred to as A2 phase, can be induced (Figure 1, irradiated areas).^[8,9,16] This phase transition is accompanied by an increased nearest-

neighbor coordination and the onset of localized ferromagnetism in the positionally ordered and chemically disordered regions as indicated by the white arrows in Figure 1.^[8,9]

To achieve a more profound understanding of the underlying physical processes during laser-induced reordering, thin films of $\text{Fe}_{60}\text{Al}_{40}$ and $\text{Fe}_{60}\text{V}_{40}$ with a nominal thickness of 40 nm on SiO_2/Si substrates were irradiated with single ultrashort laser pulses (800 nm, 40 fs). The spatial distributions of the magnetic and optical property changes resulting from pulsed laser irradiation have been investigated optically by using Kerr-microscopy and imaging ellipsometry. High-resolution transmission electron microscopy (HRTEM) was utilized to characterize the depth-dependent positional and chemical order, while electron holography enabled the assessment of the homogeneity of laser-induced magnetization in depth. To track the dynamic processes during the transformation of the atomic structure, time- and space-resolved pump-probe reflectometry was applied. This technique measures the transient evolution of reflectance which is then used as an indicator for the occurring phase changes.

Despite their fundamentally different initial positional and chemical order, both prototype alloys exhibited a similar temporal evolution of their transient reflectances until reaching the final A2 state. Within the initial ten picoseconds post-irradiation, two distinct and abrupt changes in reflectance were observed. The comparison of the experimental observations with supporting two-temperature model simulations revealed a correspondence of the abrupt reflectance changes to the formation of a transient molten state. Furthermore, the experimental and theoretical investigations demonstrated that laser-induced magnetization requires both materials to become liquid independently of their

initial atomic structure, and both alloys are required to remain in the liquid phase for a minimum time of a few hundred picoseconds.

Thus, a pathway for laser-induced reordering, independent of the initial lattice order has been identified. Despite the different initial ordering types, this pathway leads to positionally ordered yet chemically disordered lattice states accompanied with the onset of ferromagnetism. These findings identify a technically solvable challenge, which is to provide fast cooling to enable the ps generation of ferromagnetism in thin film alloys.

2. Results

2.1. Temporal Evolution of the Laser-Induced Transient Reflectance

Time-resolved imaging pump-probe reflectometry has been applied to measure the relative change of reflectance $\Delta R/R(x, y, t)$ upon irradiation in the femtosecond to the microsecond temporal range. The transient $\Delta R/R(x, y, t)$ is measured to obtain insight into the underlying structural changes, which can significantly affect the optical properties of a material,^[4,26–28] and thus, enable to estimate the time-scales at which laser-induced reordering occurs. The resulting laser-induced magnetic and structural properties of the $\text{Fe}_{60}\text{Al}_{40}$ and $\text{Fe}_{60}\text{V}_{40}$ films after irradiation are then discussed in the following Sections 2.2 and 2.3.

Since the initial reflectance of both samples before irradiation is slightly different with $R_{\text{FeAl}} = 0.47$ and $R_{\text{FeV}} = 0.57$ (see Section S.I, Supporting Information) and thus, the energy absorption upon irradiation differs, in all further considerations, the applied peak fluence F_0 of the incident pump radiation is normalized to the ablation threshold fluence $F_{\text{abl, FeAl}} = 0.16 \text{ J cm}^{-2}$ for $\text{Fe}_{60}\text{Al}_{40}$ and $F_{\text{abl, FeV}} = 0.18 \text{ J cm}^{-2}$ for $\text{Fe}_{60}\text{V}_{40}$, respectively. The determination of F_{abl} for both samples is explained in detail in Section S.II, Supporting Information. After the irradiation of both samples below the determined ablation threshold fluence, no modifications of the sample surfaces were measurable, as demonstrated in Section S.III, Supporting Information. For investigating the transient $\Delta R/R(x, y, t)$, the $\text{Fe}_{60}\text{Al}_{40}$ and $\text{Fe}_{60}\text{V}_{40}$ samples were irradiated with single pulses of pump laser radiation (800 nm, 40 fs) at $F_0 \approx 0.95 F_{\text{abl, FeAl}}$ for $\text{Fe}_{60}\text{Al}_{40}$ and $F_0 \approx 0.90 F_{\text{abl, FeV}}$ for $\text{Fe}_{60}\text{V}_{40}$. The fluence of the probe radiation (532 nm, 40 fs) is $F_0 \approx 10^{-4} F_{\text{abl}}$. The resulting spatially resolved relative change of reflectance $\Delta R/R(x, y, t)$ is demonstrated in Figure 2a,d for selected times t . In the case of $\text{Fe}_{60}\text{Al}_{40}$, the measured $\Delta R/R$ increases slightly in the temporal range of $0 \leq t \leq 2$ ps, increases even more at $t = 7$ ps, and subsequently evolves into an annular spatial distribution with a minimum in the center of the irradiated area and a surrounding annular local maximum within the temporal range of $10 \text{ ps} < t < 500 \text{ ps}$. In contrast, the measured spatially resolved $\Delta R/R(x, y, t)$ of $\text{Fe}_{60}\text{V}_{40}$ decreases upon irradiation. A similar strong decrease of $\Delta R/R(x, y)$ in the center of the irradiated area is detected in the temporal range of $20 \text{ ps} < t < 70 \text{ ps}$.

The cross-sections of $\Delta R/R(x, y, t)$ at $x = 0$ (exemplary demonstrated as white dashed line in Figure 2d) are plotted as a function of time in Figure 2b,e. By considering a Gaussian shaped spatial fluence distribution of the exciting laser radiation with the beam dimensions $w_{0,x} = 29.6 \mu\text{m}$ and $w_{0,y} = 23.0 \mu\text{m}$ at the sample sur-

face, a local fluence $F(x, y) = F_0 \cdot \exp[-2(x^2/w_{0,x}^2 + y^2/w_{0,y}^2)]$ can be assigned to each spatial coordinate. This allows for plotting the measured $\Delta R/R(y, t)$ as a function of the local fluence with $\Delta R/R(F, t)$ (see mirrored ordinate in Figure 2b,e). The beam dimensions of the exciting laser radiation are determined by the method of the squared diameter,^[29] which is explained in detail in Section S.II, Supporting Information. Since the peak fluence of the exciting pump radiation is slightly below F_{abl} , the abruptly decreasing $\Delta R/R$ in the center of the irradiated area at $10 \text{ ps} < t < 500 \text{ ps}$ for $\text{Fe}_{60}\text{Al}_{40}$ and $10 \text{ ps} < t < 100 \text{ ps}$ for $\text{Fe}_{60}\text{V}_{40}$ most probably results from a temporary delamination of the thin films, producing a cavity between the delaminated film and the material remaining on the substrate. This cavity leads to a phase shift between the probe radiation being partially reflected on the delaminated and remaining material, which can lead to the evolution of Newton rings.^[13,14,30] Since the surfaces of both films have not been modified after irradiation, the oscillating reflectance in the center of the irradiated area between $10 \text{ ps} < t < 500 \text{ ps}$ results from a temporary delamination with a subsequent reattachment of the films. Because ablation is not the scope of this study, the evolution of $\Delta R/R$ in the center is not considered more detailed in the following considerations. The three dashed lines in Figure 2b,e correspond to different local fluences F of the pump radiation, being the peak fluence $F = F_0$ (blue dashed line), the magnetization threshold $F = F_{\text{mag}}$ (green dashed line), and one fluence in between $F = 0.6 F_{\text{abl}}$ (orange dashed line). The determination of the magnetization thresholds F_{mag} is demonstrated in the following Section 2.2 resulting in $F_{\text{mag}} = 0.40 F_{\text{abl, FeAl}}$ for $\text{Fe}_{60}\text{Al}_{40}$ and $F_{\text{mag}} = 0.50 F_{\text{abl, FeV}}$ for $\text{Fe}_{60}\text{V}_{40}$ (Figure 3b,d). The measured $\Delta R/R(F, t)$ of these three fluences is plotted in Figure 2c,f. Since $\Delta R/R(F = F_0, t)$ is affected by the onset of the ablation dynamics and $\Delta R/R(F = F_{\text{mag}}, t)$ only features a small signal-to-noise ratio, the following discussion mainly focuses on $\Delta R/R$ at the fluence $F = 0.6 F_{\text{abl}}$ (orange).

In the case of $\text{Fe}_{60}\text{Al}_{40}$ (Figure 2c, orange), the measured $\Delta R/R$ increases slightly after the excitation with pump radiation (Figure 2c, red pulse) and remains at an approximately constant value of $\Delta R/R(0.6 F_{\text{abl, FeAl}}) = 0.03$ at $1 \text{ ps} < t < 3 \text{ ps}$. For $t > 3 \text{ ps}$, $\Delta R/R(0.6 F_{\text{abl, FeAl}})$ abruptly increases once again and reaches a maximum value of $\Delta R/R(0.6 F_{\text{abl, FeAl}}) = 0.1$ at $t \approx 12 \text{ ps}$. These two separate increases have been highlighted by the Roman numerals I and II as a reference for later discussions. After that, $\Delta R/R(0.6 F_{\text{abl, FeAl}})$ monotonically decreases until a final value of $\Delta R/R(0.6 F_{\text{abl, FeAl}}) \approx 0.02$ is reached at $t > 10 \mu\text{s}$, which is similar to the value measured ex situ in Figure 3b.

In the case of $\text{Fe}_{60}\text{V}_{40}$ (Figure 2f, orange), the measured $\Delta R/R$ decreases after the excitation with pump radiation (Figure 2f, red pulse) and reaches a local minimum of approximately $\Delta R/R(0.6 F_{\text{abl, FeV}}) = -0.05$ at $t = 1 \text{ ps}$ (Figure 2f, I). For $t > 1 \text{ ps}$, $\Delta R/R$ increases slightly and then abruptly decreases once again at $t > 2 \text{ ps}$ (Figure 2f, II). At $t \approx 9 \text{ ps}$ $\Delta R/R(0.6 F_{\text{abl, FeV}})$ reaches its global minimum, monotonically increases afterwards, and remains constant at later times $t > 10 \text{ ns}$.

2.2. Laser-Induced Magnetic and Optical Properties

The fluence dependent laser-induced magnetization of the samples after irradiation is obtained by considering the measured

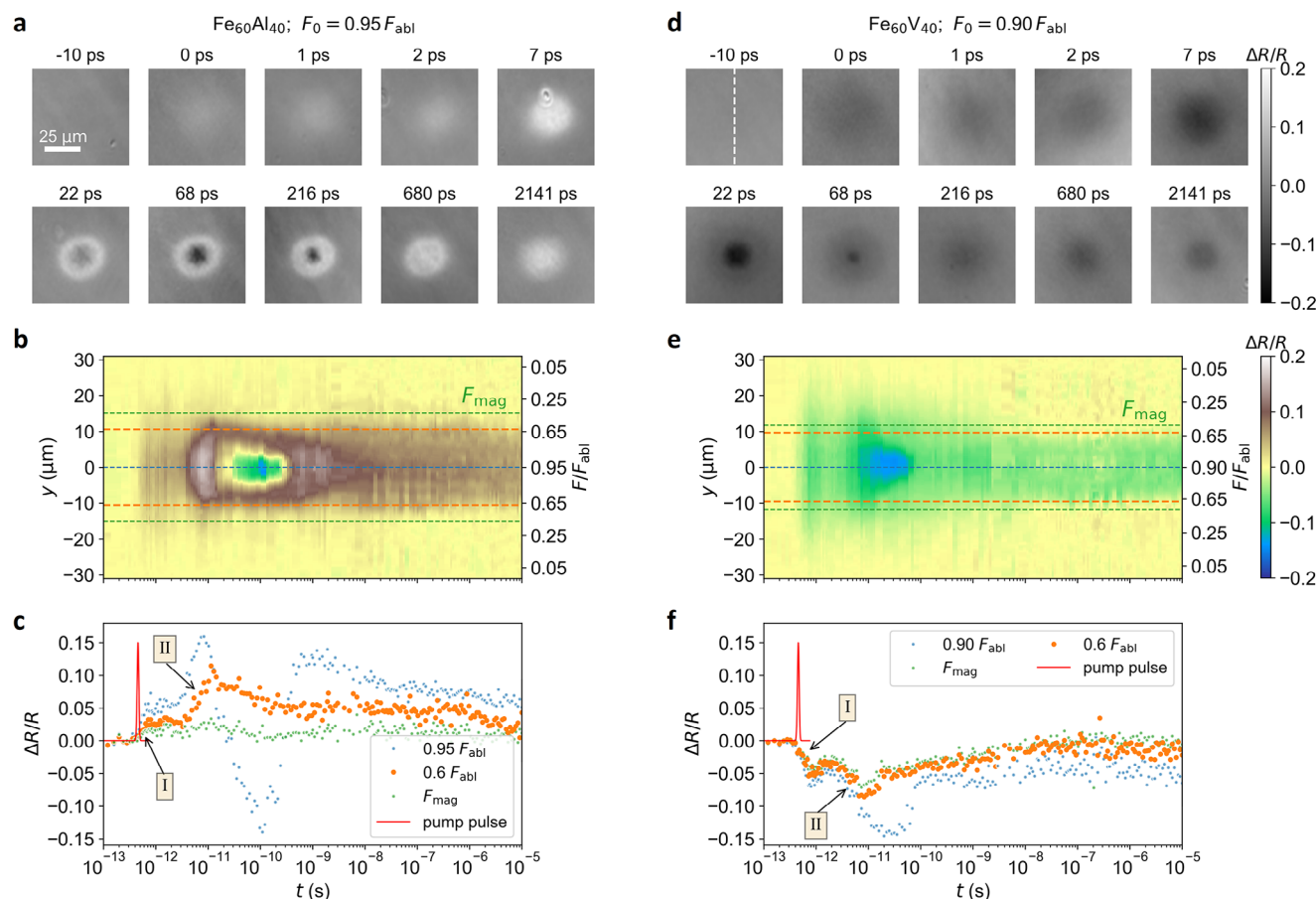


Figure 2. a,d) Spatially resolved relative change of reflectance $\Delta R/R$ of $\text{Fe}_{60}\text{Al}_{40}$ (left) and $\text{Fe}_{60}\text{V}_{40}$ (right) at different time steps measured by pump-probe reflectometry after excitation with pump radiation (800 nm, 40 fs) below the damage threshold fluence F_{abl} ; all images have the same axis scaling (see white bar at -10 ps); b,e) Cross-section of $\Delta R/R$ (along the white dashed line seen in (d)) as a function of time compared to the measured magnetization threshold fluence F_{mag} (green dashed line); c,f) Relative change of the reflectance $\Delta R/R$ as a function of time at different local fluences F of the applied pump radiation. One time-resolved measurement consists of 200 different time steps. $\Delta R/R$ has been measured three times at each time step. The mean value of the measured data at each time step is visualized by a single dot. For the sake of clarity, the standard deviation is not demonstrated here. The standard deviation corresponding to the measured data is given in Section S.VIII, Supporting Information. The red curve represents the temporal intensity distribution of the exciting pump radiation. The maximum pump intensity interacts with the sample at the time $t = 460$ fs.

normalized Kerr signal as a function of the spatial coordinates x and y . Similar to Figure 2b,d, a local fluence is assigned to each spatial coordinate by considering the Gaussian shaped spatial fluence distribution of the exciting laser radiation (Figure 3a,c, blue arrows). This allows us to plot the measured spatially resolved Kerr signal as a function of the local fluence (Figure 3b,d). The resulting fluence-resolved Kerr signal has been compared for different peak fluences $0.6 F_{\text{abl}} \leq F_0 \leq 1.15 F_{\text{abl}}$ (Figure 3b,d), demonstrating that its slope is independent of F_0 and only depends on the local fluence F . Consequently, any lateral broadening of the magnetized area due to heat diffusion after irradiation is negligible. The fluence-resolved normalized Kerr signal allows to define a magnetization threshold fluence $F_{\text{mag}} = 0.40 F_{\text{abl, FeAl}}$ for $\text{Fe}_{60}\text{Al}_{40}$ and $F_{\text{mag}} = 0.50 F_{\text{abl, FeV}}$ for $\text{Fe}_{60}\text{V}_{40}$ (Figure 3, dashed green lines), being independent of the peak fluence F_0 . In this study, the magnetization threshold F_{mag} is defined as the fluence at which the normalized Kerr signal reaches a value of $e^{-2} \approx 13.5\%$ (Figure 3b,d, green dashed lines). The normalized Kerr signal of both $\text{Fe}_{60}\text{Al}_{40}$ and $\text{Fe}_{60}\text{V}_{40}$ abruptly increases at F

$> F_{\text{mag}}$. In the case of $\text{Fe}_{60}\text{Al}_{40}$, the maximum of the Kerr signal is reached at $F \approx 0.6 F_{\text{abl, FeAl}}$ and slightly decreases again until $F = F_{\text{abl, FeAl}}$. In the case of $\text{Fe}_{60}\text{V}_{40}$, the maximum of the Kerr signal also amounts to $F \approx 0.6 F_{\text{abl, FeV}}$ and remains approximately constant between $0.6 F_{\text{abl, FeV}} < F \leq F_{\text{abl, FeV}}$.

The changed Kerr signal due to the laser-induced magnetization after irradiation is also accompanied by a changed complex refractive index, and thus a changed reflectance of both samples (Figure 3a,c). The spatially resolved complex refractive index of the samples, consisting of the refractive index and the extinction coefficient, was measured by imaging ellipsometry and allows for calculating the relative change of reflectance $\Delta R/R = (R_1 - R_0)/R_0$ of the samples, with R_0 and R_1 being the reflectances before and after irradiation, respectively. In the case of $\text{Fe}_{60}\text{Al}_{40}$, the laser-induced magnetization at fluences $F > F_{\text{mag}}$ is accompanied by an increased $\Delta R/R$, while $\Delta R/R$ of the $\text{Fe}_{60}\text{V}_{40}$ sample decreases at $F > F_{\text{mag}}$. This opposite change in their reflectances could potentially be attributed to the differing densities of states of metallic Al and V,^[31,32] thereby extending to $\text{Fe}_{60}\text{Al}_{40}$ and $\text{Fe}_{60}\text{V}_{40}$ as

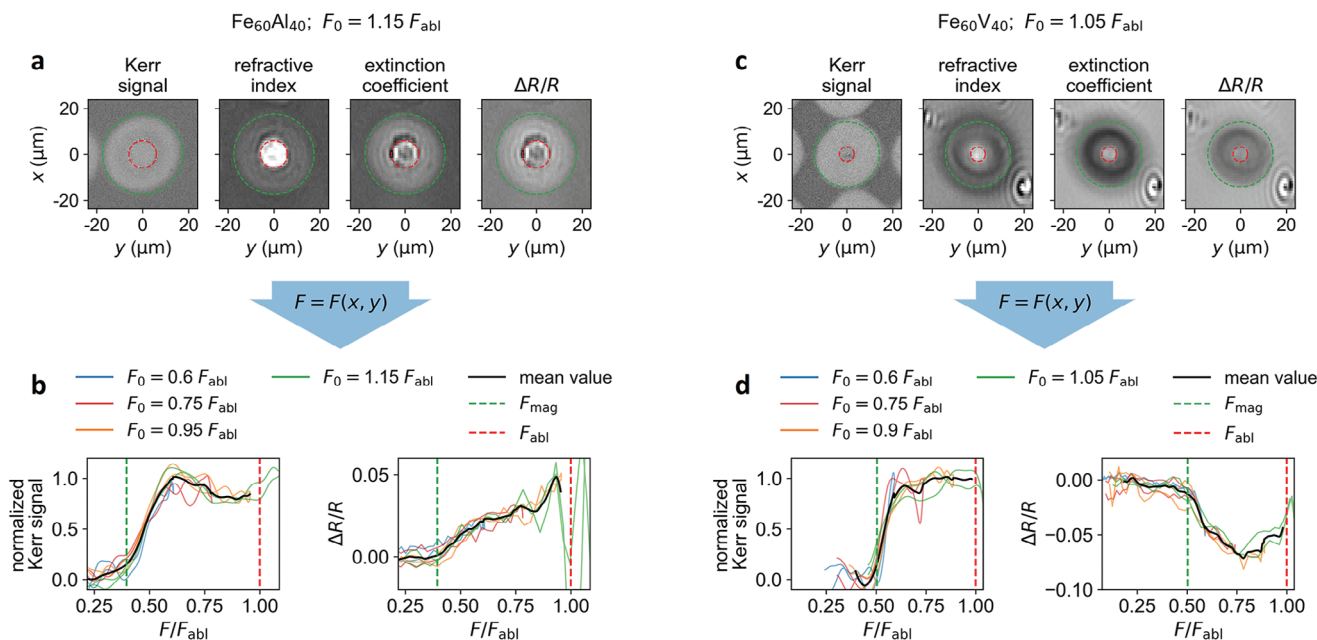


Figure 3. a, c) Spatially resolved Kerr signal (measured by Kerr microscopy), refractive index, extinction coefficient, and relative change of the reflectance $\Delta R/R$ (measured by imaging ellipsometry) of $\text{Fe}_{60}\text{Al}_{40}$ (left) and $\text{Fe}_{60}\text{V}_{40}$ (right); blue arrows: the defined Gaussian fluence distribution $F = F(x, y)$ allows to assign a local fluence to each spatial coordinate; b, d) Normalized Kerr signal (at $\mu_0 H = 20$ mT) and the relative change of reflectance $\Delta R/R$ of $\text{Fe}_{60}\text{Al}_{40}$ (left) and $\text{Fe}_{60}\text{V}_{40}$ (right) as a function of the local fluence of the exciting laser radiation; the dashed lines indicate the threshold fluences for magnetization (green dashed) and damage of the sample surface (red dashed).

well. This most probably leads to different inducible electronic transitions after laser treatment. However, the simulation of the material's optical properties depending on its atomic structure is not the scope of this article. Since the irradiation of the samples below their ablation threshold fluence does not induce any measurable modification of the sample surfaces (Section S.III, Supporting Information), the measured change of the optical properties after irradiation at $F < F_{\text{abl}}$ is not affected by any geometrical changes of the sample surface.

2.3. Local Microstructure and Magnetism of the Reordered States

In the case of $\text{Fe}_{60}\text{Al}_{40}$, both the as-grown unirradiated and the irradiated regions feature a crystalline atomic structure being positionally ordered (Figure 4a,b). Different overlapping single crystals were found in the unirradiated area which result in overlapping diffraction patterns in the fast Fourier transformation (FFT) of a $7.5 \times 7.5 \text{ nm}^2$ region (Figure 4a, blue dashed square). The FFT of the irradiated region (Figure 4b, red dashed square, $11.9 \times 11.9 \text{ nm}^2$) allows to clearly identifying isolated crystals within the thin film. In the case of $\text{Fe}_{60}\text{V}_{40}$, the unirradiated thin film displays the expected positionally disordered atomic structure with the FFT of the $11.9 \times 11.9 \text{ nm}^2$ region (Figure 4e, blue dashed square) featuring a diffuse diffraction pattern corresponding to a disordered material (Figure 4e, FFT). However, a few small crystalline grains ($< 5 \text{ nm}$) are still observable (Figure 4e, dashed orange area), which may trigger the crystallization process by acting as nucleation points during the localized laser irradiation. Similar to the irradiated $\text{Fe}_{60}\text{Al}_{40}$, the $\text{Fe}_{60}\text{V}_{40}$ sample features a positionally ordered crystalline atomic structure indicated by the pro-

nounced peaks in the diffraction pattern of the $11.9 \times 11.9 \text{ nm}^2$ region after irradiation (Figure 4f, red dashed square). However, the density and the superposition of the different crystals with individual orientations hinder the exact grain size quantification. The compositional homogeneity of the unirradiated $\text{Fe}_{60}\text{Al}_{40}$ and $\text{Fe}_{60}\text{V}_{40}$ films was preserved after laser irradiation (Section S.IV, Supporting Information), in comparison with longer laser pulse durations, where segregation is observed.^[33] Additionally to the HRTEM images demonstrated in Figure 4, further HRTEM images of the irradiated and the unirradiated areas as well as the transition area between them are shown in Section S.V, Supporting Information.

The local magnetic properties of the $\text{Fe}_{60}\text{Al}_{40}$ and $\text{Fe}_{60}\text{V}_{40}$ thin films were analyzed by off axis electron holography after laser irradiation (Figure 4c,g). Electron holography enables to extract the magnetic phase shift induced by the local electromagnetic fields created by a material at the nanoscale.^[34] The magnetic induction maps and flux line distributions were extracted in the remanent states of the thin films. Both $\text{Fe}_{60}\text{Al}_{40}$ and $\text{Fe}_{60}\text{V}_{40}$ exhibit a homogeneous singledomain-type magnetic flux distribution pointing along the thin film after laser irradiation, indicating laser-induced ferromagnetism (Figure 4c,g). The magnetic flux is oriented parallel to the substrate due to the high shape anisotropy of the prepared lamella. The well-defined magnetic phase contrast observed in Figure 4c,g is consistent with the ferromagnetic behavior measured in previous studies,^[7,8] thereby evidencing the predominant presence of chemical disorder within the irradiated area in both cases. The reference electron holography measurement of the unirradiated area reveals no detectable magnetic flux lines as demonstrated in Section S.V, Supporting Information.

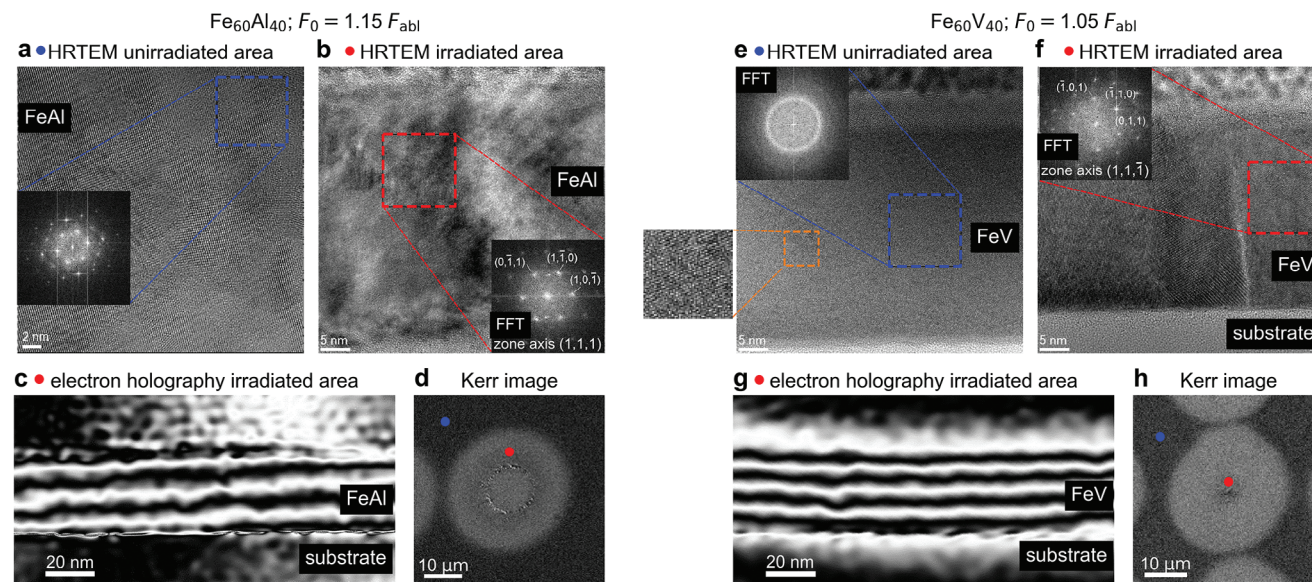


Figure 4. a,b,e,f) HRTEM images of the as-grown unirradiated $\text{Fe}_{60}\text{Al}_{40}$ (a,e) and $\text{Fe}_{60}\text{V}_{40}$ thin films and the corresponding irradiated area (b,f). The insets demonstrate the FFT images of the small selected regions. c,g) Magnetic flux distribution measured by off-axis electron holography of the annealed $\text{Fe}_{60}\text{Al}_{40}$ and $\text{Fe}_{60}\text{V}_{40}$ thin films by amplifying the cosine four times the magnetic field. d,h) The blue and red dots placed in the Kerr images indicate the location of the unirradiated (blue) and irradiated (red) areas used for the HRTEM and electron holography measurements.

2.4. Simulation of the Laser-Induced Electron and Phonon Temperature

In order to gain insight into the underlying physical processes driving the temporal evolution of $\Delta R/R$, the electron $T_e(t)$ and phonon temperatures $T_p(t)$ obtained from TTM simulations are compared with the experimental data. It should be emphasized that simulating the transient optical properties during laser-induced heating is a complex task that falls beyond the scope of this article. Therefore, following discussion relies on a qualitative comparison between the measured $\Delta R/R$ and the simulated $T_e(t)$ and $T_p(t)$, along with the observed correlations.

For both samples (Figure 5a,d), the qualitative comparison of the measured $\Delta R/R$ with the simulated electron temperature $T_e(t)$ and phonon temperature $T_p(t)$ of the sample surface indicates that the first change of $\Delta R/R$ (increase for $\text{Fe}_{60}\text{Al}_{40}$, decrease for $\text{Fe}_{60}\text{V}_{40}$) within the first picosecond after excitation predominantly results from the excitation of the electron system, as the slopes of $\Delta R/R$ and $T_e(t)$ are comparable in this temporal range, while the phonon temperature exhibits a considerably slower rise than the electron temperature. Thus, the first change of $\Delta R/R$ (Figure 5, I) results from a broadening of the Fermi distribution in both materials, which transiently enables or inhibits optical transitions resulting in a changed reflectance.^[11,13]

The phonon temperature $T_p(t)$ increases slightly delayed due to the time needed for the electron-phonon coupling.^[13,15,35,36] The second significantly more pronounced change of $\Delta R/R$ at $t > 3$ ps becomes apparent only after $T_p(t)$ has exceeded the melting temperature and the materials have liquefied. Given that the electron temperature starts decreasing for $t > 0.7$ ps, this second change of the reflectance is certainly caused by the dynamics in the phonon system. A variation in the phonon dispersion relation due to heating or liquefaction also strongly affects the

dispersion relation of the electrons and their optical transitions, respectively.^[37] The absence of a third abrupt change of $\Delta R/R$ in the whole considered temporal range (Figure 2) makes it challenging to clearly define the moment when the material freezes again by considering only the time-resolved measurements. The reason for this might be attributed to different heating and cooling rates, as the heating results from the ultrafast laser excitation and the electron-phonon coupling, while the cooling is primarily driven by the slower heat conduction into the surrounding unirradiated area. Therefore, the TTM simulations are necessary to estimate the time scale at which the phase transitions occur for both $\text{Fe}_{60}\text{Al}_{40}$ and $\text{Fe}_{60}\text{V}_{40}$.

The comparison of the simulated maximum phonon temperature as a function of the exciting laser fluence with the magnetization threshold fluence F_{mag} (Figure 5b,e) implies that the laser-induced magnetization is achievable only when the material becomes temporarily liquid. The simulated phonon temperature crosses the melting temperature approximately 1 ps after irradiation the earliest. However, the simulated resolidification time demonstrates that laser-induced magnetization requires a minimum time of approximately 200 picoseconds for $\text{Fe}_{60}\text{Al}_{40}$ as well as $\text{Fe}_{60}\text{V}_{40}$ to endure in the liquid phase (Figure 5c,f). The resolidification time is defined as the moment when the phonon temperature of the sample surface falls below the melting point. The temporal evolutions of the temperature gradients in depth and the corresponding phase states are demonstrated in Section S.IX, Supporting Information. Considering Figure 5c,f leads to two conclusions. First, laser-induced magnetization requires the material to become liquid independently of the initial atomic structure. Second, both alloys are required to remain in the liquid phase for a minimum time of approximately 200 ps, so that the transition to the positionally ordered and chemically disordered A2 phase and the accompanied ferromagnetism can develop after

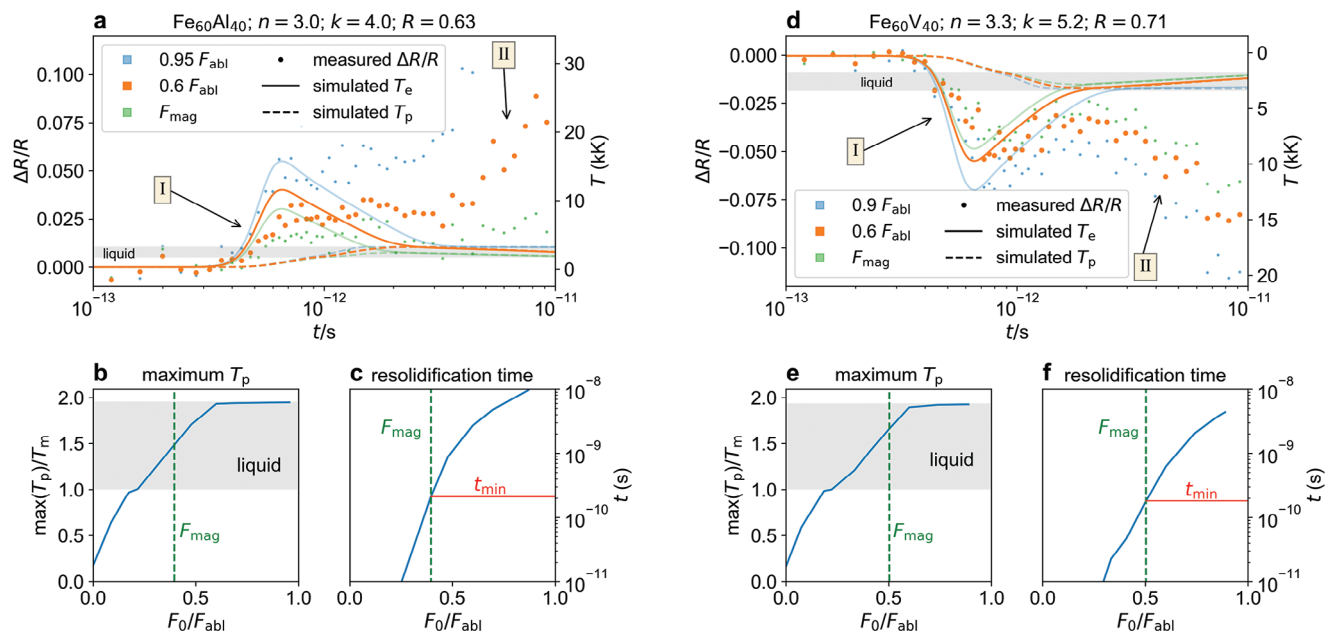


Figure 5. a, d) Qualitative comparison of the measured $\Delta R/R$ of the irradiated Fe₆₀Al₄₀ (left) and Fe₆₀V₄₀ (right) samples with the electron T_e and phonon temperature T_p being simulated by a two-temperature model for different fluences of the pump radiation relative to the measured damage threshold fluence F_{abl} ; the given refractive index n , extinction coefficient k , and the reflectance R used as input parameters for the simulations were measured at rest using ellipsometry. b, e) Maximum simulated phonon temperature T_p after irradiation as a function of the applied fluence. c, f) Resolidification time as a function of the applied fluence, representing the time needed for Fe₆₀Al₄₀ (left) and Fe₆₀V₄₀ (right) to cool down below the melting temperature $T < T_m$ after being previously excited above T_m .

resolidification (Figure 5c,f, red line t_{min}). The maximum resolidification time is controllable by the applied laser radiation fluence. Since the observed temporal evolution of $\Delta R/R$ is quite similar for both Fe₆₀Al₄₀ and Fe₆₀V₄₀, the initial positional and chemical order of the atomic species has negligible impact on the final induced atomic rearrangement. Therefore, the heating and cooling rates, being affected by the parameters of the applied laser radiation (pulse duration, fluence, and beam dimensions) as well as the thermophysical properties of the material, play a much more crucial role for the atomic rearrangement.

3. Conclusion

The dynamics of the laser-induced atomic reordering processes in the two prototype alloy systems, Fe₆₀Al₄₀ and Fe₆₀V₄₀, were tracked by time-resolved observations of the transient reflectance. Prior to irradiation, both alloys were in a non-ferromagnetic state, however differed vastly in their initial lattice orders. Fe₆₀Al₄₀ exhibited a crystalline atomic structure with both positional and chemical order, while Fe₆₀V₄₀ was positionally and chemically disordered. After single-pulsed femtosecond laser irradiation (800 nm, 40 fs), both alloys underwent an atomic rearrangement, leading to a positionally ordered structure with a chemical disorder of the atomic species. These rearrangements were accompanied by the emergence of ferromagnetism and were achieved without damaging the sample surfaces. By comparing the measured relative change of reflectance after irradiation with simulations of the electron and phonon temperatures, it was determined that both alloys needed to be transiently liquefied for a minimum duration of approximately 200 ps for the transition to the posi-

tionally ordered and chemically disordered phase state, as well as the development of magnetization, to occur upon resolidification. Therefore, the laser-induced atomic reordering and magnetization were found to be independent of the atomic structure of the precursor alloy before irradiation, but highly depend on the pulse duration and fluence of the applied laser radiation and may be further controllable through fs multi-pulse sequences.

As the local functionalization of materials using fs laser pulsing, achieved purely through lattice reordering, is currently being pursued in a variety of alloy systems,^[38–40] understanding the limits of such transformations in various material systems is crucial for developing novel techniques in the modulation of functional properties.

4. Experimental Section

Sample Preparation: Thin films of Fe₆₀Al₄₀ and Fe₆₀V₄₀ were prepared on SiO₂ (270 nm)/Si (001) substrates. Both materials were prepared using DC magnetron sputtering from targets of the corresponding compositions. The chamber base pressure was 2×10^{-9} mbar and film growth was performed in an Ar-atmpsohere of 3×10^{-3} mbar. The growth rate was kept at 0.6 \AA s^{-1} , to obtain nominal film thicknesses of $d_f = 40$ nm. The Fe₆₀Al₄₀ films were grown at 300 K and subsequently annealed at 773 K in a vacuum to obtain the B2 structure.^[8] In the case of Fe₆₀V₄₀, the films were grown while maintaining a substrate temperature of 773 K, giving an optimized short-range ordered phase.^[10] Film thicknesses were calibrated using X-ray reflectivity, where a 4 nm thick oxide layer formation can be deduced from fitting of the Kiessing fringes and directly observed using transmission electron microscopy. The structure of the as-prepared films was confirmed by grazing incidence X-ray diffraction the occurrence of the 100 superstructure reflection confirmed the formation of B2 ordering in

$\text{Fe}_{60}\text{Al}_{40}$ and the absence of diffraction reflections and the presence of a broad peak in $\text{Fe}_{60}\text{V}_{40}$. Within the instrumental resolution the as-prepared as well as laser treated films of both alloys were observed to be compositionally homogeneous, as seen using TEM based EDX. Additional details of the thin-film growth and characterization of the ordered structure have been published previously.^[8,9]

Kerr Microscopy: A Kerr microscope from Evico Magnetics (Germany) was used for magnetic imaging.^[41] The sample surface was illuminated with polarized light and the contrast contained a magnetic component due to the rotation of polarization by the magnetized regions (magneto-optical Kerr effect, MOKE). Images were recorded while applying a magnetic field aligned longitudinally with the optical polarization axis. To separate the magnetic contrast from the optical, a reference background image was obtained by averaging images taken while applying positive and negative saturating magnetic fields, respectively. Subtracting the background image from the images recorded in fixed magnetic fields removed the optical contrast component, which was field independent, thereby giving the change in magnetic contrast with respect to the background. Hysteresis loops were obtained by averaging the contrast change over single magnetic regions, recorded while sweeping the field in steps. Kerr microscopy images of the samples after irradiation at different peak fluences and the corresponding hysteresis loops are demonstrated in Section S.VI, Supporting Information.

Imaging Ellipsometry: The spatially resolved complex refractive index of the samples was measured by a commercial imaging ellipsometer (nanofilm_ep4, Accurion) at the wavelength 532 nm. The used objective had a numerical aperture of $N_A = 0.35$ resulting in a spatial resolution of $\Delta x \approx 1.5 \mu\text{m}$.

Micro-Structural Analysis by TEM: High resolution transmission electron microscopy (HRTEM) imaging was performed in an FEI Titan Cube 60-300 system operated at 300 kV and fitted with a Schottky field emission gun (S-FEG), a CETCOR aberration corrector for an objective lens from CEOS providing subangstrom point resolution, and a bottom-mounted $2\text{K} \times 2\text{K}$ Ultrascan CCD camera from Gatan.

Off-Axis Electron Holography: The magnetization of the $\text{Fe}_{60}\text{Al}_{40}$ and $\text{Fe}_{60}\text{V}_{40}$ thin films was analyzed by off-axis electron holography carried out in the same FEI Titan Cube 60-300 operated at 300 kV. For this purpose, the instrument was also equipped with a S-FEG, a motorized electrostatic biprism, and a Lorentz lens. The experiments were performed in Lorentz mode, that is, with the objective lens switched off, and the Lorentz lens operating as the image-forming lens. The excitation of the biprism was set to 150 V to produce holograms with a fringe contrast above 15%. The acquisition time of the holograms was 4 s. The holograms were acquired at remanence, after saturating the magnetization in two opposite directions along the longitudinal axis of the lamellae. Therefore, the electrostatic phase shift (which conserves its sign upon magnetization reversal) could be subtracted to obtain the magnetic phase shift. Saturation was achieved by tilting the long axis of the lamellae by 30° and exciting the objective lens, so that an axial magnetic field of 0.3 T was obtained. The magnetic flux distribution had been obtained by amplifying the cosine of four times the magnetic phase.

Imaging Pump-Probe Reflectometry: An amplified Ti:sapphire femtosecond laser system (Astrella, Coherent Inc., $\lambda = 800 \text{ nm}$, $\tau_H = 35 \text{ fs}$, $M^2 = 1.2$) provided ultrashort pulsed laser radiation, which was divided into pump and probe radiation by a beam splitter. The wavelength of the probe radiation was changed to 532 nm using an optical parametric amplifier (TOPAS Prime, Light Conversion Inc.). The pump radiation was focused onto the sample surface by a thin focusing lens ($f = 150 \text{ mm}$) at an angle of incidence of 50° and a parallel polarization state relative to the plane of incidence. The resulting beam dimensions on the material surface were $w_{0,x} = 29.6 \mu\text{m}$ and $w_{0,y} = 23.0 \mu\text{m}$, being determined by the method of the squared diameter.^[29] The spatial, spectral, and temporal properties of the pump and probe radiation in the femtosecond regime were characterized in detail in a previous publication.^[12] During the interaction of the pump radiation with the thin $\text{Fe}_{60}\text{Al}_{40}$ and $\text{Fe}_{60}\text{V}_{40}$ films, the relative change of reflectance $\Delta R/R$ was measured by pump-probe reflectometry with an angle of incidence of 0° of the probe radiation. The optical beam paths of the pump and probe radiation were changed rela-

tively to each other by a geometrical delay stage, resulting in a temporal range of $-0.5 \text{ ns} < t < 3 \text{ ns}$ with a minimum temporal step width of $\Delta t = 40 \text{ fs}$. In order to observe $\Delta R/R$ of the thin films at later times after irradiation, a second radiation source ($\lambda = 532 \text{ nm}$, $\tau_H = 2.7 \text{ ns}$, $M^2 = 1.2$) could be used to provide the probe radiation. In this mode, the two radiation sources (fs-pump and ns-probe) were temporally delayed relatively to each other by an external delay generator, resulting in a temporal range of $0 < t < 100 \mu\text{s}$ with a minimum temporal step width of $\Delta t = 3 \text{ ns}$. The temporal intensity distribution of the probe radiation in the nanosecond regime is demonstrated in Section S.VII, Supporting Information. The pump-probe reflectometer was combined with an imaging setup consisting of a microscope objective ($20\times$, $N_A = 0.4$), a tube lens ($f = 200 \text{ mm}$), and a CCD-camera (1024×1024 pixel, pixel size $4.8 \mu\text{m} \times 4.8 \mu\text{m}$), enabling to measure $\Delta R/R$ spatially resolved with a lateral resolution of $\Delta x \approx 1.3 \mu\text{m}$ at 532 nm wavelength. As the experiments were performed above or just slightly below the ablation threshold fluence, an unmodified area of the sample surface has to be irradiated and imaged for every single time step. Therefore, the sample was repositioned by an automated x-y axes system. A detailed explanation of the experimental setup is provided in Section S.VIII, Supporting Information.

One time-resolved measurement (as presented in Figure 2) consisted of 200 different time steps. $\Delta R/R$ had been measured three times at each time step. The mean value of the measured data at each time step was visualized by a single dot. For the sake of clarity, the corresponding standard deviation was not demonstrated in the figures of the main article. The standard deviation is shown in Section S.VIII, Supporting Information.

Two-Temperature Model Simulation: The temporal evolution of the electron temperature $T_e(t)$ as well as the phonon temperature $T_p(t)$ of the thin films upon excitation by ultrashort pulsed laser radiation was calculated by a 1D two-temperature model for different fluences. The exact procedure as well as the temperature dependent thermophysical parameters are explained in Section S.IX, Supporting Information.

Statistical Analysis: The methods used for evaluating the measured data are described in Section 4. No additional statistical methods had been applied.

Supporting Information

Supporting Information is available from the Wiley Online Library or from the author.

Acknowledgements

T.P., M.O., and A.H. gratefully thank the Deutsche Forschungsgemeinschaft (DFG) for funding the Major Research Instrumentation No. INST 522/14-1 FUGG and the project No. 469106482. M.S.A. and R.B. acknowledge funding from the Deutsche Forschungsgemeinschaft (DFG), project No. 322462997 (BA 5656/1-2|WE 2623/14-2). J.P.-N., C.M., and M.R.I. gratefully thank the European Union's Horizon 2020 research and innovation program for the grant agreement No. 823717-ESTEEM3, and the regional Gobierno de Aragón for projects E13_23R and E28_23R. The authors thank Heiko Wende and Olav Hellwig for productive discussions.

Open access funding enabled and organized by Projekt DEAL.

Conflict of Interest

The authors declare no conflict of interest.

Data Availability Statement

The data that support the findings of this study are available from the corresponding author upon reasonable request.

Keywords

atomic reordering, chemical order, ferrimagnetism, positional order, pump-probe reflectometry

Received: October 5, 2023
Revised: November 6, 2023
Published online:

- [1] C. Yun, J. W. Han, S. Kim, D. C. Lim, H. Jung, S.-H. Lee, J.-W. Jang, S. Yoo, K. Leo, Y. H. Kim, *Mater. Horiz.* **2019**, *6*, 2143.
- [2] C. Florian, D. Fischer, K. Freiberg, M. Duwe, M. Sahre, S. Schneider, A. Hertwig, J. Krüger, M. Rettenmayr, U. Beck, A. Undisz, J. Bonse, *Materials (Basel, Switzerland)* **2021**, *14*, 7.
- [3] I. Choi, H. Y. Jeong, H. Shin, G. Kang, M. Byun, H. Kim, A. M. Chitu, J. S. Im, R. S. Ruoff, S.-Y. Choi, K. J. Lee, *Nat. Commun.* **2016**, *7*, 13562.
- [4] T. Pflug, A. Anand, S. Busse, M. Olbrich, U. S. Schubert, H. Hoppe, A. Horn, *ACS Appl. Electron. Mater.* **2021**, *3*, 2825.
- [5] M. Cardona, P. Fulde, H.-J. Queisser, *Topological Disorder in Condensed Matter* (Eds: F. Yonezawa, T. Ninomiya), Springer Series in Solid-State Sciences, Vol. 46, Springer, Berlin, Heidelberg **1983**.
- [6] J. K. Christie, S. N. Taraskin, S. R. Elliott, *J. Phys.: Condens. Matter* **2004**, *16*, S5109.
- [7] M. Arslan, C. Bese, Z. Tabak, T. Bozdog, E. Duman, H. G. Yaglioglu, *J. Appl. Phys.* **2022**, *131*, 093904.
- [8] R. Bali, S. Wintz, F. Meutzner, R. Hübner, R. Boucher, A. A. Ünal, S. Valencia, A. Neudert, K. Potzger, J. Bauch, F. Kronast, S. Facsko, J. Lindner, J. Fassbender, *Nano Lett.* **2014**, *14*, 435.
- [9] J. Ehrler, M. He, M. V. Shugaev, N. I. Polushkin, S. Wintz, V. Liersch, S. Cornelius, R. Hübner, K. Potzger, J. Lindner, J. Fassbender, A. A. Ünal, S. Valencia, F. Kronast, L. V. Zhigilei, R. Bali, *ACS Appl. Mater. Interfaces* **2018**, *10*, 15232.
- [10] M. S. Anwar, H. Cansever, B. Boehm, R. A. Gallardo, R. Hübner, S. Zhou, U. Kentsch, S. Rauls, B. Eggert, H. Wende, K. Potzger, J. Fassbender, K. Lenz, J. Lindner, O. Hellwig, R. Bali, *ACS Appl. Electron. Mater.* **2022**, *4*, 3860.
- [11] T. Pflug, J. Wang, M. Olbrich, M. Frank, A. Horn, *Appl. Phys. A* **2018**, *124*, 17572.
- [12] T. Pflug, M. Olbrich, A. Horn, *Phys. Rev. B* **2022**, *106*, 1307.
- [13] T. Pflug, M. Olbrich, J. Winter, J. Schille, U. Löschner, H. Huber, A. Horn, *J. Phys. Chem. C* **2021**, *125*, 17363.
- [14] J. Winter, S. Rapp, M. Spellaug, C. Eulenkamp, M. Schmidt, H. P. Huber, *Appl. Surf. Sci.* **2020**, *511*, 145514.
- [15] M. Olbrich, T. Pflug, C. Wüstefeld, M. Motylenko, S. Sandfeld, D. Rafaja, A. Horn, *Opt. Lasers Eng.* **2020**, *129*, 106067.
- [16] M. Andreeva, A. Smekhova, R. Baulin, Y. Repchenko, R. Bali, C. Schmitz-Antoniak, H. Wende, I. Sergueev, K. Schlage, H. C. Wille, *J. Synchrotron Radiat.* **2021**, *28*, 1535.
- [17] F. Röder, G. Hlawacek, S. Wintz, R. Hübner, L. Bischoff, H. Lichte, K. Potzger, J. Lindner, J. Fassbender, R. Bali, *Sci. Rep.* **2015**, *5*, 16786.
- [18] J. C. Krause, J. Schaf, M. I. Da Costa, C. Paduani, *Phys. Rev. B: Condens. Matter* **2000**, *61*, 6196.
- [19] M. Bałanda, S. M. Dubiel, R. Pełka, *J. Magn. Magn. Mater.* **2017**, *432*, 430.
- [20] J.-I. Seki, M. Hagiwara, T. Suzuki, *J. Mater. Sci.* **1979**, *14*, 2404.
- [21] N. Kataoka, K. Sumiyama, Y. Nakamura, *Trans. Jpn. Inst. Met.* **1986**, *27*, 823.
- [22] J. Ehrler, B. Sanyal, J. Grenzer, S. Zhou, R. Böttger, B. Eggert, H. Wende, J. Lindner, J. Fassbender, C. Leyens, K. Potzger, R. Bali, *New J. Phys.* **2020**, *22*, 073004.
- [23] M. Nord, A. Semisalova, A. Kákay, G. Hlawacek, I. MacLaren, V. Liersch, O. M. Volkov, D. Makarov, G. W. Paterson, K. Potzger, J. Lindner, J. Fassbender, D. McGrouther, R. Bali, *Small* **2019**, *15*, 1970287.
- [24] E. Menéndez, M. O. Liedke, J. Fassbender, T. Gemming, A. Weber, L. J. Heyderman, K. V. Rao, S. C. Deevi, S. Suriñach, M. D. Baró, J. Sort, J. Nogués, *Small* **2009**, *5*, 229.
- [25] Y. Yoshida, K. Oosawa, S. Watanabe, H. Kaiju, K. Kondo, A. Ishibashi, K. Yoshimi, *Appl. Phys. Lett.* **2013**, *102*, 18.
- [26] D. E. Aspnes, A. A. Studna, *Phys. Rev. B* **1983**, *27*, 985.
- [27] D. T. Pierce, W. E. Spicer, *Phys. Rev. B* **1972**, *5*, 3017.
- [28] M. Magnozzi, T. Pflug, M. Ferrera, S. Pace, L. Ramó, M. Olbrich, P. Canepa, H. Ağircan, A. Horn, S. Forti, O. Cavalleri, C. Coletti, F. Bisio, M. Canepa, *J. Phys. Chem. C* **2021**, *121*, 16059.
- [29] J. M. Liu, *Opt. Lett.* **1982**, *7*, 196.
- [30] F. Meyer, *Ph.D. Dissertation*, Albert-Ludwigs-Universität Freiburg im Breisgau **2021**.
- [31] T. Zhang, G. Y. Guo, *Phys. Rev. B* **2005**, *71*, 21.
- [32] T. Genieys, M. Sentis, O. Utéza, *Appl. Phys. A* **2020**, *126*, 88.
- [33] N. I. Polushkin, A. C. Duarte, O. Conde, E. Alves, N. P. Barradas, A. García-García, G. N. Kakazei, J. O. Ventura, J. P. Araujo, V. Oliveira, R. Vilar, *Appl. Surf. Sci.* **2015**, *336*, 380.
- [34] E. Snoeck, C. Gatel, in *Transmission Electron Microscopy in Micro-Nanoelectronics* (Eds: A. Claverie, M. Mouis), Vol. 115, John Wiley & Sons, Inc, Hoboken, NJ **2012**, pp. 107–134.
- [35] M. Olbrich, E. Punzel, P. Lickschat, S. Weißmantel, A. Horn, *Phys. Proc.* **2016**, *83*, 93.
- [36] J. Hohlfeld, S.-S. Wellershoff, J. Güdde, U. Conrad, V. Jähnke, E. Matthias, *Chem. Phys.* **2000**, *251*, 237.
- [37] V. Recoules, J. Clérouin, G. Zérah, P. M. Anglade, S. Mazevet, *Phys. Rev. Lett.* **2006**, *96*, 055503.
- [38] D. G. Merkel, K. Sájerman, T. Váczi, S. Lenk, G. Hegedűs, S. Sajti, A. Németh, M. A. Gracheva, P. Petrik, D. Mukherjee, Z. E. Horváth, D. L. Nagy, A. Lengyel, *Mater. Res. Express* **2023**, *10*, 076101.
- [39] M. Deb, E. Popova, S. P. Zeuschner, W. Leitenberger, N. Keller, M. Rössle, M. Bargheer, *Phys. Rev. B* **2021**, *103*, 6.
- [40] Y. Meng, J. K. Behera, Z. Wang, J. Zheng, J. Wei, L. Wu, Y. Wang, *Appl. Surf. Sci.* **2020**, *508*, 145228.
- [41] A. Hubert, R. Schäfer, *Magnetic Domains: The Analysis of Magnetic Microstructures*, Springer, Berlin, Heidelberg **1998**.